ISSN 1674-1056
http://cpb.iphy.ac.cn
http://iopscience.iop.org/cpb
中国物理 B
Chinese Physics
中国物理 Chinese Physics B

Enhanced dielectric and optical properties of nanoscale barium hexaferrites for optoelectronics and high frequency application

Mohammed J, Suleiman A B, Tchouank Tekou Carol T, Hafeez H Y, Sharma J, Maji Pradip K, Kumar Sachin Godara, Srivastava A K

Citation: Chin. Phys. B . 2018, 27(12): 128104. **doi:** 10.1088/1674-1056/27/12/128104
Journal homepage: http://cpb.iphy.ac.cn; http://iopscience.iop.org/cpb

What follows is a list of articles you may be interested in

In situ growth of different numbers of gold nanoparticles on MoS_2 with enhanced electrocatalytic activity for hydrogen evolution reaction

Xuan Zhao(赵宣), Da-Wei He(何大伟), Yong-Sheng Wang(王永生), Chen Fu(付晨)
Chin. Phys. B . 2018, 27(6): 068103. **doi:** 10.1088/1674-1056/27/6/068103

Nucleation mechanism and morphology evolution of MoS_2 flakes grown by chemical vapor deposition

He-Ju Xu(许贺菊), Jian-Song Mi(米建松), Yun Li(李云), Bin Zhang(张彬), Ri-Dong Cong(丛日东), Guang-Sheng Fu(傅广生), Wei Yu(于威)
Chin. Phys. B . 2017, 26(12): 128102. **doi:** 10.1088/1674-1056/26/12/128102

Magnetoelectric effect in multiferroic $NdMn_2O_5$

Syed Hamad Bukhari, Javed Ahmad
Chin. Phys. B . 2017, 26(1): 018103. **doi:** 10.1088/1674-1056/26/1/018103

Influences of different structures on the characteristics of H_2O-based and O_3-based La_xAl_yO films deposited by atomic layer deposition

Chen-Xi Fei(费晨曦), Hong-Xia Liu(刘红侠), Xing Wang(汪星), Dong-Dong Zhao(赵冬冬), Shu-Long Wang(王树龙), Shu-Peng Chen(陈树鹏)
Chin. Phys. B . 2016, 25(5): 058106. **doi:** 10.1088/1674-1056/25/5/058106

Formation of $ZnGa_2O_4$ films by multilayer deposition and subsequent thermal annealing

Yan Jin-Liang, Zhao Yin-Nü, Li Chao
Chin. Phys. B . 2014, 23(4): 048105. **doi:** 10.1088/1674-1056/23/4/048105

Enhanced dielectric and optical properties of nanoscale barium hexaferrites for optoelectronics and high frequency application

J Mohammed[1,2], A B Suleiman[2], Tchouank Tekou Carol T[1], H Y Hafeez[2,3], Jyoti Sharma[1], Pradip K Maji[4], Sachin Godara Kumar[5], and A K Srivastava[1,†]

[1] *Department of Physics, School of Chemical Engineering and Physical Sciences, Lovely Professional University, Phagwara-144411, Punjab, India*
[2] *Department of Physics, Faculty of Science, Federal University Dutse, P M B 7156, Dutse, Jigawa state, Nigeria*
[3] *SRM Research Institute, SRM University, Kattankulathur 603203, Chennai, India*
[4] *Department of Polymer and Processing Engineering, Indian Institute of Technology Roorkee, Saharanpur Campus, Saharanpur-247001, U P, India*
[5] *Department of Chemistry, Guru Nanak Dev University, Amritsa-143005, India*

(Received 6 August 2018; revised manuscript received 26 September 2018; published online 10 November 2018)

M-type barium hexaferrites with chemical composition $Ba_{1-x}Dy_xFe_{12-y}Cr_yO_{19}$ ($x = 0.0, 0.1, 0.2$, and $y = 0.0, 0.4, 0.5$) were synthesized via sol–gel auto-combustion method. The samples were pre-sintered at 400 °C for 3 h and sintered at 950 °C for 5 h. The changes in the structural, dielectric, and optical properties were studied after the substitution of Dy^{3+} and Cr^{3+} ions. X-ray diffraction (XRD) analysis confirms the formation of single phase hexaferrites with the absence of secondary phase. FTIR analysis gives an idea of the formation of hexaferrites with the appearance of two peaks at 438 cm^{-1} and 589 cm^{-1}. The field emission scanning electron micrographs (FESEM) show a combination of crystallites with large shapes close to hexagonal platelet-like shape and others with rice or rod-like shapes, whereas EDX and elemental analysis confirm the stoichiometry of prepared samples. The calculated band gap from UV-vis NIR spectroscopy spectra was found to decreases with increase in Dy^{3+}–Cr^{3+} substitution. The dielectric properties were explained on the basis of Maxwell–Wagner model. Enhancement of dielectric constant at higher frequencies was observed in all the samples. Low dielectric loss is also observed in all the samples and Cole–Cole plot shows that grain boundary resistance (R_{gb}) contribute most to the dielectric properties. The prepared samples exhibit properties that could be useful for optoelectronics and high frequency application.

Keywords: Maxwell–Wagner model, dielectric constant, Cole–Cole plot, optical band-gap

PACS: 81.07.Bc, 77.22.Gm, 77.22.Ch, 77.22.–d **DOI:** 10.1088/1674-1056/27/12/128104

1. Introduction

The past few decades have witnessed a tremendous exploration of magnetic materials as a result of their attractive applications in areas such as high frequency technology, absorption of electromagnetic waves, magnetic refrigerator technology, magnetic recording media, and electro–optical devices.[1–6] Hexaferrites are known to be chemically stable, inexpensive and friendly to the environment, which makes them viable candidates for various technological applications.[7–9] The variants of hexaferrites include M-type, Y-type, U-type, W-type, X-type, and Z-type, their corresponding chemical compositions are, respectively, $BaFe_{12}O_{19}$, $Ba_2Me_2Fe_{12}O_{22}$, $Ba_4Me_2Fe_{36}O_{60}$, $Ba_2Me_2Fe_{16}O_{27}$, $Ba_2Me_2Fe_{28}O_{46}$, and $Ba_3Me_2Fe_{24}O_{41}$, where Me_2 represents a small divalent ion such as cobalt, nickel, zinc or magnesium, strontium or lead may replace the barium.[10] M-type hexaferrites exhibit much better properties and it is easy to synthesize at lower temperatures without the occurrence of secondary phase, such as magnetite (–Fe_2O_3).[11] M-type hexaferrites possessed magnetoplumbite structure with space group $P6_3/mmc$ and a unit cell consisting of 2 Ba^{2+}, 24 Fe^{3+}, and 38 O^{2+} ions. The magnetoplumbite structure consists of a dual layer having RSR^*S^* stacking sequence. The R and R^* stacking sequence consist of hexagonal structure having three distinct layers of oxygen, whereas the S and S^* stacking sequence consists of a spinel structure having two different layers of oxygen, the asterisk shows the 180° rotation of that particular stacking sequence.[12]

The properties of hexaferrites depend on factors such as chemical composition, synthesis method, calcination temperature, and duration, nature of substituted ions, impurity and crystallite size.[7,13] Hexaferrites have been synthesized with variety of methods such as micro-emulsion, solid state reaction method, and co-precipitation method. However, the sol–gel method offers several advantages such as compositional homogeneity, low reaction temperature, and time.[14] Usually, the dielectric constant rapidly decreases at low frequency and exhibit frequency independent behavior at intermediate and higher frequencies. El-Sayed *et al*. synthesized Al-substituted M-type barium hexaferrites using solid state reaction method and observed that the dielectric constant increases with temperature at lower frequencies while temperature independent behavior was observed at higher frequencies.[15] Naeem *et al*. observed an abrupt decrease of dielectric constant at lower frequencies and frequency independent behavior at higher frequencies in Zr–Cd substituted strontium hexaferrites pre-

†Corresponding author. E-mail: srivastava_phy@yahoo.co.in
© 2018 Chinese Physical Society and IOP Publishing Ltd

pared by the sol–gel method.[16] The optical band-gap may decrease or increase depending on the nature of the substituted ions and characterization method. Kaur *et al*. studied the magnetic properties and determined the optical band-gap of sol–gel synthesized Gd–Co substituted hexaferrites using UV-vis NIR spectroscopy, the observed optical band-gap ranges from 4.07 eV to 4.28 eV, the optical band-gap initially decreases with substitution and then later increases.[17] Auwal *et al.* studied the magnetic, hyperfine interactions, and optical properties of La-substituted hexaferrites synthesized by the sol–gel method using diffuse reflectance spectrophotometer (DRS), the calculated band gap falls in the range 1.34 eV to 1.78 eV.[18]

Taking inspiration from the literature review, this work aimed to synthesized Dy^{3+}–Cr^{3+}substituted barium hexaferrites using the sol–gel auto-combustion method and investigates the role of Dy^{3+} and Cr^{3+} ions on the dielectric and optical properties. The prepared samples were characterized using x-ray diffraction (XRD), Fourier transform infrared spectroscopy (FTIR), FE-SEM/EDX, and elemental analysis, UV-Vis-NIR spectrophotometer, and impedance analyzer.

2. Experimental details

The sol–gel method was applied to synthesize M-type barium hexaferrites with chemical composition $Ba_{1-x}Dy_xFe_{12-y}Cr_yO_{19}$ ($x = 0.0, 0.1, 0.2$, and $y = 0.0, 0.4, 0.5$), as shown in Table 1. The starting materials used were of analytic reagent grade such as $Ba(NO_3)_2$ (Loba Chemie), $Cr(NO_3)_3{\cdot}9H_2O$ (Loba Chemie), $Fe(NO_3)_3{\cdot}9H_2O$ (Loba Chemie), $DyN_3O_9 \cdot xH_2O$ (Sigma-Aldrich), and citric acid (Loba Chemie) having 98%–99% purity. Stoichiometric amounts of the starting materials were weighed and dissolved in water to form the salt solution, required amount of citric acid was added to the salt solution with cations to citric acid molar ratio maintained at 1:1.5, respectively. Ammonia solution was added drop wise to adjust the pH of the salt solution to 7.00. The solution was placed on a magnetic stirrer and stirred at 80 °C–100 °C, much of the water was evaporated and a brown gel was formed, which upon further heating at 280 °C–300 °C gives the precursor material. The precursor material was pre-sintered at 400 °C for 3 h and sintered at 950 °C for 5 h.

Table 1. The sample composition and code for $Ba_{1-x}Dy_xFe_{12-y}Cr_yO_{19}$ ($x = 0.0$, 0.1, 0.2, and $y = 0.0, 0.4, 0.5$).

x	y	Sample composition	Sample code
0.0	0.0	$BaFe_{12}O_{19}$	B1
0.1	0.4	$Ba_{0.9}Dy_{0.1}Fe_{11.6}Cr_{0.4}O_{19}$	B2
0.2	0.5	$Ba_{0.8}Dy_{0.2}Fe_{11.5}Cr_{0.5}O_{19}$	B3

3. Characterization techniques

The structural analysis was carried out with x-ray diffraction pattern obtained in the range 20°–80° using Cu–K radiation operating at 40 kV and 35 mA with step size 0.02° (Bruker AXS D8 advance diffractometer). The attached functional groups were investigated with Fourier transform infrared (FTIR) spectrometer (Nicolet FTIR interferometer IR prestige-21 (model-8400S)). The sample was mixed with KBr in the ratio 1:10, respectively, after which thin pellets of 1-mm thickness were made and spectra was recorded in the wavenumber range 4000 cm^{-1} and 400 cm^{-1}. Topology and elemental analysis of the prepared sample was carried out with field emission scanning electron microscopy (FE-SEM, MIRA3 TESCAN, USA) operated at 5-mm working distance and accelerating voltage of 5 kV to 10 kV. Band-gap (E_g) of the prepared sample was studied using UV-Vis-NIR spectrophotometer (Varian, Cary 5000 with spectral range of 175 nm–3300 nm). Dielectric properties in the frequency range 20 Hz to 120 MHz was investigated using impedance analyzer (Wayne Kerr 6500B) with 0-V to +40-V DC bias voltage and 0-mA to 100-mA DC bias current, pellets of 4-mm thickness was prepared and coated with silver conducting paint prior to the dielectric measurement.

4. Results and discussion

4.1. X-ray diffraction analysis

Figure 1 presents the x-ray diffraction (XRD) spectra of M-type barium hexagonal ferrites with chemical composition $Ba_{1-x}Dy_xFe_{12-y}Cr_yO_{19}$ ($x = 0.0, 0.1, 0.2$, and $y = 0.0, 0.4, 0.5$). The XRD spectra show well-defined intense and sharp peaks with *hkl* values (006), (110), (008), (107), (114), (200), (203), (109), (205), (206), (1011), (209), (217), (304), (2011), (2012), (220), (2014), and (317), this indicates the formation of a crystalline hexagonal ferrites phase with no secondary phase such as α-Fe_2O_3 and the successful substitution of Dy^{3+} and Cr^{3+} in the M-type hexagonal structure. The XRD spectra were indexed according to standard JCPDS Card No. 39-1433 and were found to be identical to unsubstituted $BaFe_{12}O_{19}$ with space group $P6_3/mmc$. The values of lattice parameters (a and c), crystallite size (D), volume of unit cell (V_{cell}), and strain (η) were calculated using Eqs. (1), (2), (3), and (4) respectively, and presented in Table 2.

$$\frac{1}{d_{hkl}^2} = \frac{4}{3}\left(\frac{h^2+hk+l^2}{a^2}\right) + \frac{l^2}{c^2}, \tag{1}$$

$$D = \frac{k\lambda}{\beta\cos\theta}, \tag{2}$$

$$V_{cell} = 0.8666a^2c, \tag{3}$$

$$\eta = \frac{\beta\cos\theta - 0.9\lambda/D}{2\sin\theta}, \tag{4}$$

where d_{hkl} is the value of d spacing, *hkl* are the miller indices, β (in radian) is the full width at half maximum, θ is the Braggs angle, k is the shape factor which has a value of 1 for hexagonal ferrites, and λ is the x-ray wavelength having a value of 1.54056 Å. From Table 2, it can be seen that a, c, and V_{cell} decrease with Dy^{3+}–Cr^{3+} substitution, this could

be explained on the basis of the ionic radius of the substituted ions. It has been reported that the values of a, c, and V_{cell} may decrease if the ionic radii of the substituted ions are smaller than those of the host ions and *vice versa*. The ionic radius of Dy^{3+} (1.03 Å) is smaller than that of Ba^{2+} (1.35 Å); similarly, the ionic radius of Cr^{3+} (0.52 Å) is also smaller than that of Fe^{3+} (0.64 Å).[13,14,19–21] This scenario prompts the distortion of the unit cell thereby causing microstructural defects and strain, consequently resulting in the observed decreased a, c, and V_{cell} values. The c/a ratio varies slightly with Dy^{3+}–Cr^{3+} substitution and maintained an approximate value of 3.94 for all samples (Table 2). It has been reported that if the ratio is below 3.98, then the prepared sample can be assumed to exhibit hexagonal structure.[22,23] Since the c/a ratio is less than 3.98 for all synthesized samples, we can assume that the prepared samples exhibit hexagonal structure. The values of crystallite size do not follow a regular pattern with Dy^{3+}–Cr^{3+} substitution (Table 2), and it increases for the sample B2 and decreases for B3. The unsubstituted sample, *i.e.* B1 exhibits the lowest crystallite size (22.91 nm). The strain (η) that is distortion-induced during the synthesis process shows a decreasing behavior with Dy^{3+}–Cr^{3+} substitution, this may be due to enhancement towards pure phase of hexaferrites.[24]

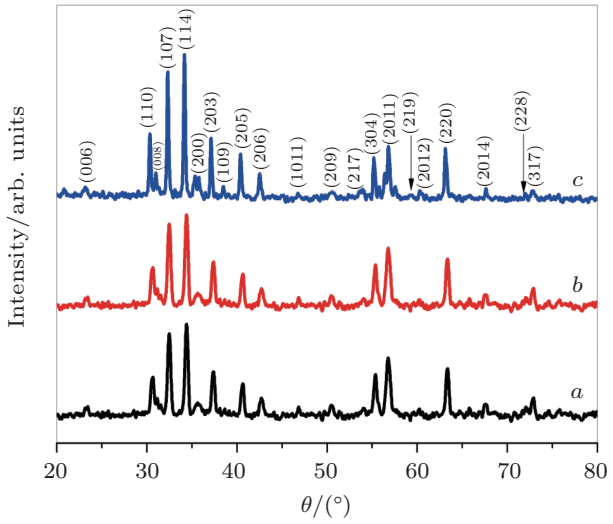


Fig. 1. (color online) XRD patterns of $Ba_{1-x}Dy_xFe_{12-y}Cr_yO_{19}$ ($x = 0.0$, 0.1, 0.2, and $y = 0.0$, 0.4, 0.5) B1 (curve *a*), B2 (curve *b*), and B3 (curve *c*).

Table 2. Values of lattice parameters (a and c), crystallite size (D), volume of unit cell (V_{cell}), and strain (η) for $Ba_{1-x}Dy_xFe_{12-y}Cr_yO_{19}$ ($x = 0.0, 0.1, 0.2$, and $y = 0.0, 0.4, 0.5$).

x/y	2θ/(°)	d/Å	β/(°)	a/Å	c/Å	c/a	V_{cell}/Å^3	D/nm	$\eta \times 10^{-4}$
0.0/0.0	30.23	2.9541	0.399	5.90	23.27	3.9440	703.92	22.91	12.89
0.1/0.3	30.31	2.9464	0.174	5.89	23.21	3.9405	698.51	52.54	5.60
0.2/0.5	30.39	2.9015	0.235	5.87	23.15	3.9437	693.16	38.91	7.55

4.2. FTIR analysis

Figure 2 shows the room temperature FTIR spectra of $Ba_{1-x}Dy_xFe_{12-y}Cr_yO_{19}$ ($x = 0.0, 0.1, 0.2$, and $y = 0.0, 0.4, 0.5$) in the range 4000 cm^{-1} to 400 cm^{-1}. The presence of two absorption bands at 438 cm^{-1} and 589 cm^{-1} which are characteristics bands of hexaferrites gives an idea of the formation of the hexaferrite structure.[25] These bands are due to metal–oxygen stretching vibrations (such as Fe–O, Cu–O, Mg–O, and Zr–O) at the octahedral and tetrahedral sites in the hexagonal lattice.[26] The band at 438 cm^{-1} occurs in the octahedral site whereas the band at 598 cm^{-1} occurs at the tetrahedral site, the variation in Fe^{3+}–O^{2+} distances at octahedral and tetrahedral sites cause shifting of the position of the absorption bands towards lower frequency side.[27] The shifts in these absorption bands towards lower frequency occur as a result of the occupation of the substituted cations in the Fe^{3+} site, the unsubstituted sample (*i.e.*, sample B1) exhibits these bands due to the stretching vibration of Ba–O. The absorption bands in the range 1100 cm^{-1} to 1500 cm^{-1} observed in all the samples could be attributed to metal–oxygen–metal (M–O–M) bonds such as Fe–O–Fe bonds; broad absorption band observed at 3459 cm^{-1} as a result of –OH stretching vibration could be due to the presence of water molecules absorbed by the samples.[28] The observed absorption band at 1649 cm^{-1} results from H–O–H bending vibration of H_2O.[29]

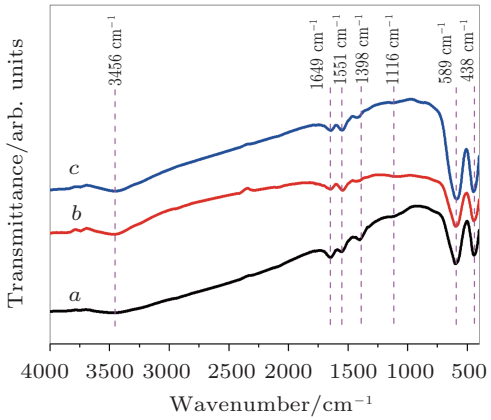


Fig. 2. (color online) FTIR spectra of $Ba_{1-x}Dy_xFe_{12-y}Cr_yO_{19}$ ($x = 0.0, 0.1, 0.2$, and $y = 0.0, 0.4, 0.5$) for B1 (curve *a*), B2 (curve *b*), and B3 (curve *c*).

4.3. FESEM, EDX, and elemental mapping

The FESEM micrographs of $Ba_{1-x}Dy_xFe_{12-y}Cr_yO_{19}$ ($x = 0.0, 0.1, 0.2$, and $y = 0.0, 0.4, 0.5$) are presented in Fig. 3. The average grain sizes for all the samples are around 0.1 m to 0.2 m as estimated from the micrographs. Since the grain sizes obtained from XRD is much smaller than those observed in FESEM, we can assume that the grains agglomerate to form larger ones in all the prepared samples. Clearly, the agglomeration is observed in all the samples which could be attributed to magnetic interaction with other neighboring grains.[30] The

micrographs show some crystallites with large shapes close to hexagonal platelet-like and others with rice or rod-like shapes. The shapes of the crystallites are vital for various applications, crystallites with large hexagonal platelet-like shapes are useful as radar absorber materials.[31,32] The crystallites with rice or rod-like shapes may find application in data storage, catalysis, imaging, sensing, and surface enhance Raman scattering.[33] The EDX and elemental analysis for the samples B2 and B3 are shown in Fig. 4. Both the EDX spectra and elemental micrographs confirm the stoichiometry of the prepared samples.

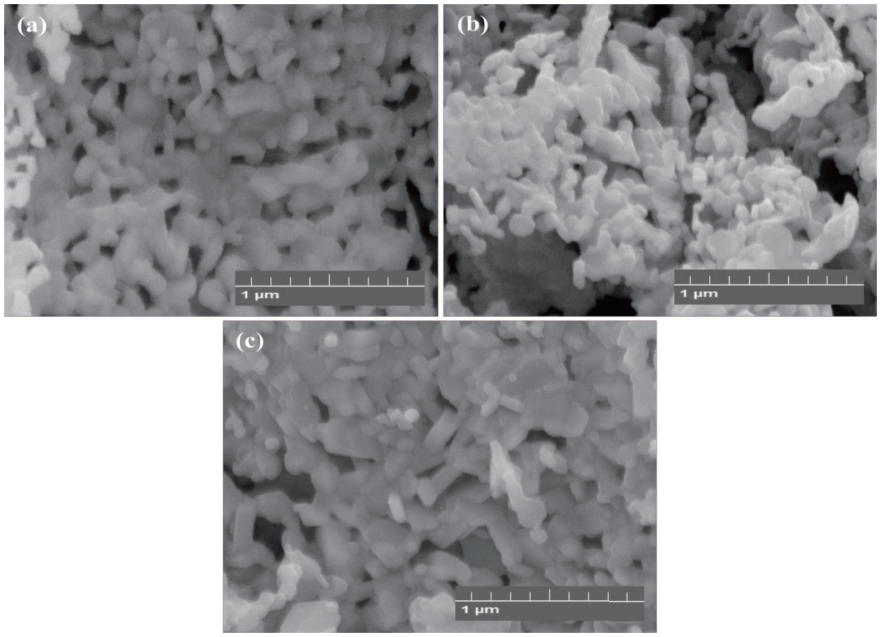


Fig. 3. (color online) The FESEM micrograph of $Ba_{1-x}Dy_xFe_{12-y}Cr_yO_{19}$ ($x = 0.0, 0.1, 0.2$, and $y = 0.0, 0.4, 0.5$) for B1 (a), B2 (b), and B3 (c).

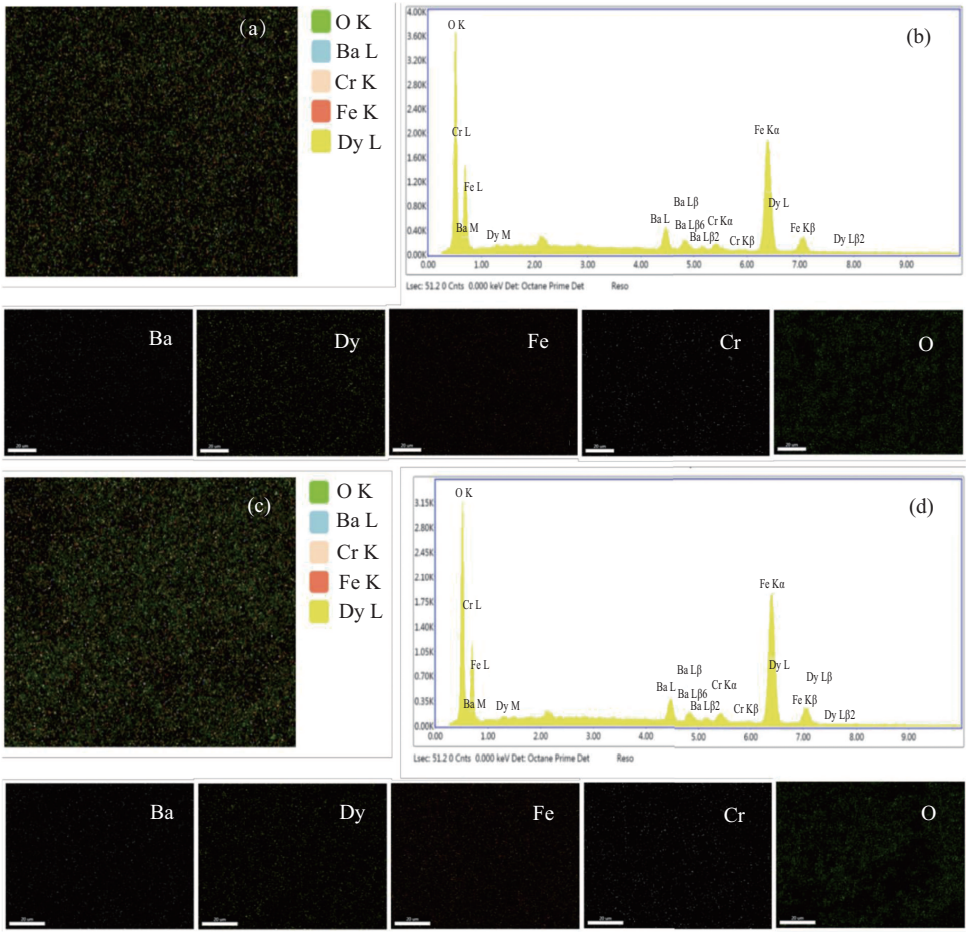


Fig. 4. (color online) The elemental mappings of samples B2 (a), B3 (b) and EDX spectra of samples B2 (c), B3 (d) for $Ba_{1-x}Dy_xFe_{12-y}Cr_yO_{19}$ ($x = 0.0, 0.1, 0.2$, and $y = 0.0, 0.4, 0.5$).

4.4. Optical analysis

In UV-vis NIR spectroscopy, the energy of incident photons is absorbed by electrons in the sample, followed by their excitation from the valence band to the conduction band. The optical properties of $Ba_{1-x}Dy_xFe_{12-y}Cr_yO_{19}$ ($x = 0.0, 0.1, 0.2$, and $y = 0.0, 0.4, 0.5$) have been investigated using UV-vis spectroscopy in the range 234 nm–766 nm. The spectra of the absorbance as a function of wavelength are presented in Fig. 5. The spectra show absorption peaks at 272, 354, 475, and 726 nm which result from σ–σ^*, n–σ^*, π–π^*, and n–π^* transitions. In addition, there were two reflection peaks observed at 418 nm and 690 nm. The reflection peak at 418 nm corresponds to hypochromic shift whereas that at 690 nm corresponds to hyperchromic shift. There is no observation of hypsochromic (blue) shift and bathochromic (red) shift in the spectra. The absorption peak at 726 nm and the reflection peak at 690 nm merge together as Dy^{3+}–Cr^{3+} is substituted, this shows that the substitution of Dy^{3+}–Cr^{3+} enhances the absorption by the prepared samples. The optical band gap (E_g) was determined using Tauc relation[34]

$$\alpha h\nu = A(h\nu - E_g)^n, \tag{5}$$

where α is the absorbance, h is the Plank constant (6.6260×10^{-34} J·s), ν is the frequency of the incident photon, and A is a characteristics constant that depends on n. The values of n are, respectively, 1/2, 3/2, 2, and 3 for allowed direct, forbidden direct, allowed indirect, and forbidden indirect transitions. Figure 6 shows the plots of E_g for the synthesized samples. The value of E_g for all the samples was evaluated by extrapolation of the linear part of the graph of $(\alpha h\nu)^2$ against E_g. The values of E_g for samples B1, B2, and B3 were found to be 2.89, 2.71, and 2.39 eV respectively.

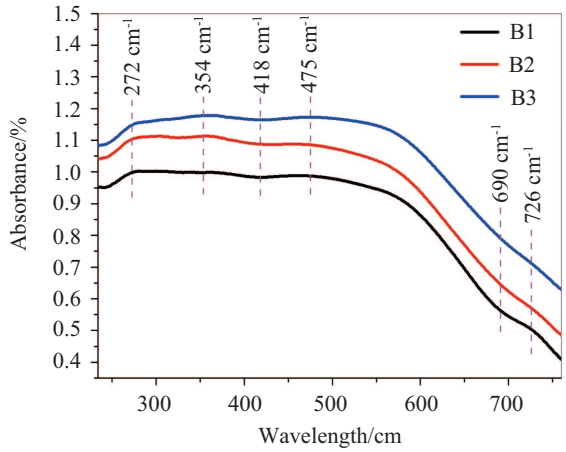


Fig. 5. (color online) Variation of absorbance versus wavelength for $Ba_{1-x}Dy_xFe_{12-y}Cr_yO_{19}$ ($x = 0.0, 0.1, 0.2$, and $y = 0.0, 0.4, 0.5$).

From Figs. 6 and 7, we can observe that E_g decreases with increases in Dy^{3+}–Cr^{3+} substitution. Kaur *et al.* observed that the variation of E_g relies on factors such as quantum confinement and crystallite size.[12] The E_g observed are higher than those obtained for strontium hexaferrites thin films prepared by laser ablation method.[35]

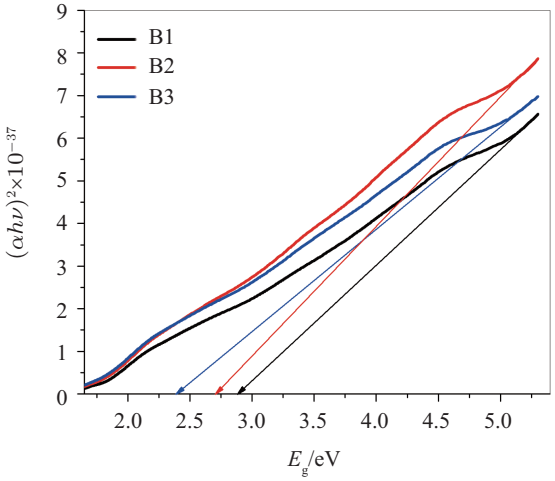


Fig. 6. (color online) Optical band gap for $Ba_{1-x}Dy_xFe_{12-y}Cr_yO_{19}$ ($x = 0.0, 0.1, 0.2$, and $y = 0.0, 0.4, 0.5$).

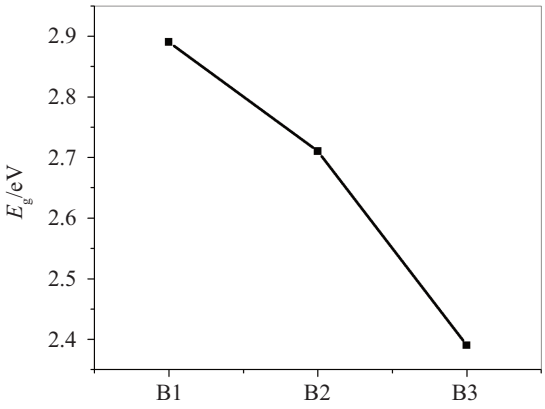


Fig. 7. Variation of band gap with Dy^{3+}–Cr^{3+} substitution.

4.5. Dielectric analysis

The response of nanomaterial to an applied electric field is better understood using impedance spectroscopy. This may present us with vital information regarding conduction mechanism involving ionic, electronic, and interfacial polarization. The parameters calculated from the impedance spectroscopy are complex permittivity (ε^*), real part of complex permittivity (ε'), and the imaginary part of complex permittivity (ε'') which are expressed in Eqs. (6), (7), and (8), respectively.[36]

$$\varepsilon^* = \varepsilon' - j\varepsilon'', \tag{6}$$

$$\varepsilon' = \frac{Z''}{2\pi\omega C_0 Z^2}, \tag{7}$$

$$\varepsilon'' = \frac{Z'}{2\pi\omega C_0 Z^2}, \tag{8}$$

where $j = \sqrt{-1}$ is an imaginary number, Z' is the real part of complex impedance, Z'' is the imaginary part of complex

impedance, $\omega = 2\pi f$ is the frequency, and C_0 is the geometrical capacitance. The complex impedance (Z^*), real part of complex impedance (Z'), and the imaginary part of complex impedance (Z'') are, respectively, given in Eqs. (9), (10), and (11)[37]

$$Z^* = Z' - \mathrm{j}Z'', \tag{9}$$

$$Z' = |Z|\cos\theta, \tag{10}$$

$$Z'' = |Z|\sin\theta, \tag{11}$$

where θ is the phase angle. The ratio of ε'' and ε' represents the dielectric loss tangent ($\tan\delta$) or energy dissipation factor of the nanomaterial.[10]

$$\tan\delta = \frac{\varepsilon''}{\varepsilon'}. \tag{12}$$

The conducting properties of a nanomaterial can be explained on the basis of the following equation[38]

$$\sigma_{\text{total}} = \sigma_{\text{ac}} + \sigma_{\text{dc}}, \tag{13}$$

where σ_{dc} is the frequency-independent part of conductivity, σ_{ac} ($\sigma_{\text{ac}} = A\omega^s$) is the frequency-dependent part of conductivity, A is the temperature-dependent constant, and s is a numerical constant. AC conductivity can be expressed by the following relation[39]

$$\sigma_{\text{ac}} = \omega\varepsilon_0\varepsilon'\tan\delta. \tag{14}$$

4.5.1. Dielectric constant

The energy storage ability of hexaferrites is better understood by analyzing ε'. Figure 8 represents the room temperature frequency-dependent ε' for $Ba_{1-x}Dy_xFe_{12-y}Cr_yO_{19}$ ($x = 0.0, 0.1, 0.2$, and $y = 0.0, 0.4, 0.5$). The dielectric properties of hexaferrites can be explained on the basis of Maxwell–Wagner model. In accordance with this model, the layers of conducting grains in ferrites is surrounded by layers of poorly conducting grain boundaries.[34] When an electric field is applied at lower frequencies, charge carriers easily migrate through the grains and accumulate at the grain boundaries which result in high interfacial polarization owing to high resistivity and consequently high values of ε'; whereas at higher frequencies, the interfacial polarization drastically decreases to negligible values. At this point, only electronic and dipolar polarization contribute to the values of ε'.[40] All the samples exhibit a high value of ε' at lower frequencies as compared with intermediate and higher frequencies, space charge polarization, oxygen vacancies, and grain boundary defects are the reason behind the high value of ε' at lower frequencies.[13] From Fig. 8, it can be observed that ε' increases with increase in Dy^{3+}–Cr^{3+} substitution for all the samples, this could be attributed to increased space charge polarization as a result enhancement in electron hopping between Fe^{3+} and Fe^{2+} ions.[41] Clearly, ε' shows a decreasing trend with increase in frequency both at lower and intermediate frequencies for all samples. At higher frequencies, there is an abrupt increase in ε', this indicates that ε' is enhanced by Dy^{3+}–Cr^{3+} substitution at higher frequencies. The increasing behavior of ε' reduces the penetration depth of EM waves by increasing the skin effect, this means that lower values of ε' observed in hexagonal ferrites as compared with the ε' of calcium copper titanate ($> 9 \times 10^3$ at 10^6 Hz) makes them useful for high frequency application.[16,42]

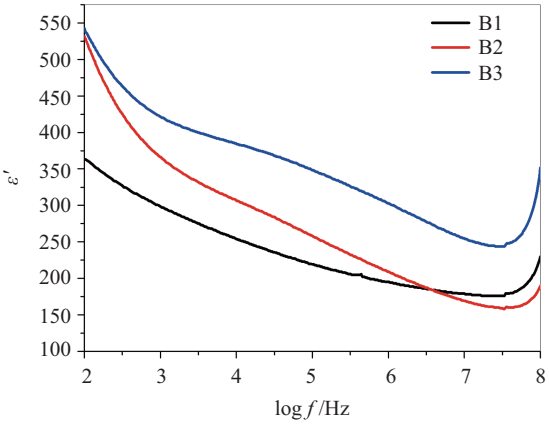


Fig. 8. (color online) Variation of room temperature real part of dielectric permittivity (ε') with frequency for $Ba_{1-x}Dy_xFe_{12-y}Cr_yO_{19}$ ($x = 0.0, 0.1, 0.2$, and $y = 0.0, 0.4, 0.5$).

4.5.2. Dielectric loss (tanδ)

The dielectric loss ($\tan\delta$) shows the nature of energy dissipation of the hexaferrite nanomaterial during the conduction of electrons in the dielectric system. Variation of with frequency at room temperature for $Ba_{1-x}Dy_xFe_{12-y}Cr_yO_{19}$ ($x = 0.0, 0.1, 0.2$, and $y = 0.0, 0.4, 0.5$) is presented in Fig. 9. Electron hopping produces polarization which varies with the applied electric field; when the polarization lags behind the applied electric field above a certain critical frequency, appears.[43] This is justified by the presence of defects (vacancies and interstitials), impurities, and structural imperfections in the material as a result of substitutions of cation with different valency and ionic radius.[14,15] The prepared samples exhibit high $\tan\delta$ at lower frequencies; this corresponds to loss of energy. There is high resistivity at lower frequencies as a result of grain boundaries; this scenario prompts the need for more energy in order for electron hopping between Fe^{3+} and Fe^{2+} ions to occur. Hence, high $\tan\delta$ (or loss of energy) is observed at lower frequencies. Less resistivity is observed at higher frequencies as a result of conducting grains and consequently less energy is required for electron hopping between Fe^{3+} and Fe^{2+} ions to occur. Thus, small $\tan\delta$ (or loss of energy) is observed at higher frequencies.[13,16] The contribution

to $\tan\delta$ at lower frequencies could be attributed to hopping conduction of electrons whereas the observed $\tan\delta$ at higher frequencies could be due to the response of defect dipoles to the applied electric field, the defect dipoles arise during the process of calcination as a result of the transition of Fe^{3+} ions to Fe^{2+} ions.[44] Resonance or Debye-like relaxation peaks are observed in the samples B2 as well as in B3 at higher frequencies, these peaks occur when the frequency of electron jumping during electron exchange between Fe^{3+} and Fe^{2+} ions equals the frequency of the applied electric field.[39] The observed decrease in $\tan\delta$ after the occurrence of the Debye-like relaxation peaks in the samples B2 as well as B3 at higher frequencies can be explained on the basis of relaxation of the defects dipoles, under the influence of applied electric field the relaxation of these defects dipoles displays a decreasing behavior with increase in frequency and subsequently decreases the $\tan\delta$ in the higher frequencies side.[45]

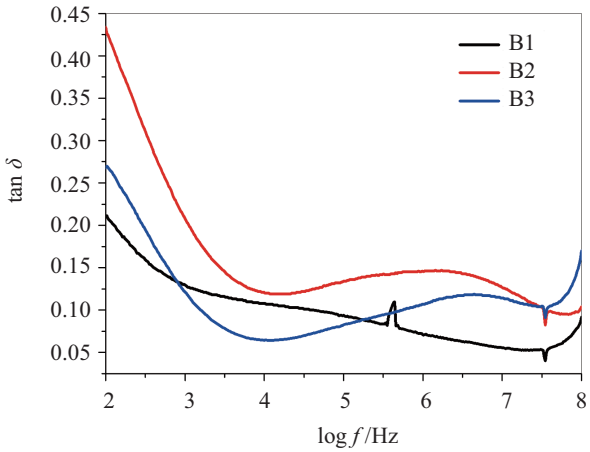


Fig. 9. (color online) Variation of dielectric loss tangent ($\tan\delta$) with frequency for $Ba_{1-x}Dy_xFe_{12-y}Cr_yO_{19}$ ($x = 0.0, 0.1, 0.2$, and $y = 0.0, 0.4, 0.5$)

4.5.3. Cole–Cole plot

The nature of the grain and grain boundary resistance of the synthesized samples can be observed from the behavior of the curve observed in Cole–Cole plot (also called Nyquist plots), which is a plot of the imaginary part (Z'') versus real part (Z') of complex impedance (Z^*). Figure 10 presents the Cole–Cole plot of $Ba_{1-x}Dy_xFe_{12-y}Cr_yO_{19}$ ($x = 0.0, 0.1, 0.2$, and $y = 0.0, 0.4, 0.5$) at room temperature. The analysis of Cole–Cole plots gives vital parameters which characterized non-Debye-like relaxation behavior.[46] A polycrystalline hexagonal ferrite sample can be thought to consist of grains (or parallel conducting plates) separated by grain boundaries (or resistive plates). A Cole–Cole plot consists of a semi-circle arc starting from the lower frequencies side to the higher frequencies side. The part of the semi-circle at the lower frequency side represents the contribution of the grain boundaries (or grain boundary resistance (R_{gb}) while the part of the semi-circle at the higher frequency side of the Cole–Cole plot represents the contribution from the grains (or grain resistance (R_g).[47] From Fig. 10, we can observe that there is no higher frequency arc for the samples B1 as well as B2. Hence, we can conclude that there is no or less contribution from R_g towards the dielectric properties for these samples. The arc for the sample B3 extends to the higher frequency side of the plot. This is an indication that there is contribution from R_g towards the dielectric properties for this sample and that the quantity of grains has increased. Consequently, we can expect the sample B3 to be more conducting than the samples B1 as well as B2 since grain boundaries are less conducting than grains. From the forgoing discussion, we can assume that R_{gb} contributes most to the dielectric properties of the synthesized samples.

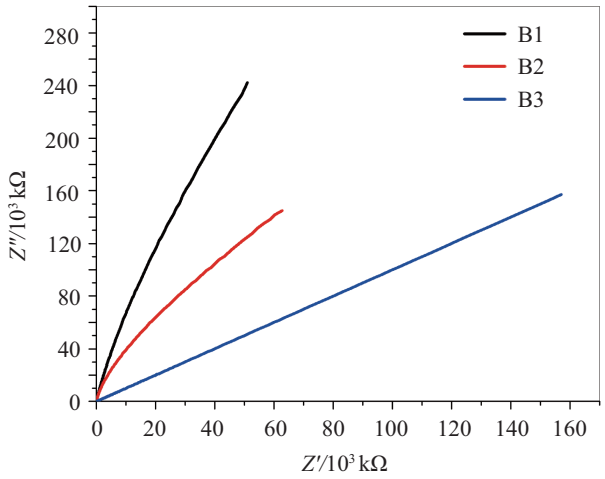


Fig. 10. (color online) Cole–Cole plot for $Ba_{1-x}Dy_xFe_{12-y}Cr_yO_{19}$ ($x = 0.0, 0.1, 0.2$, and $y = 0.0, 0.4, 0.5$).

4.5.4. AC conductivity (σ_{ac})

The AC conductivity (σ_{ac}) of $Ba_{1-x}Dy_xFe_{12-y}Cr_yO_{19}$ ($x = 0.0$, 0.1, 0.2, and $y = 0.0$, 0.4, 0.5) is presented in Fig. 11. From lower to intermediate frequencies, σ_{ac} exhibits frequency-independent behavior, this could be attributed to the presence of random distribution of charge carriers through activated electron hopping.[43] At higher frequencies, there is a sudden and abrupt rise in σ_{ac} of the prepared samples; this behavior correlates with the increase in ε' at higher frequencies (Fig. 8). Similar to the behavior of ε', the behavior of σ_{AC} of hexaferrites depends on electron hopping between Fe^{3+} and Fe^{2+} ions at octahedral site. As the frequency of the applied electric field is varied, electron hopping between Fe^{3+} and Fe^{2+} ions at octahedral site increases thereby resulting in increased conductivity.[48] The conduction mechanism in hexaferrites has been explained by assuming the process of polarization in hexaferrites to be similar to the process of conduction; in this manner, electron hopping between Fe^{3+} and

Fe^{2+} ions at octahedral site results in the occurrence of local displacement and the subsequent generation of polarization which is responsible for conduction in hexaferrites.[49,50] Similar to ε', we can conclude that Dy^{3+}–Cr^{3+} substitution enhances at higher frequencies.

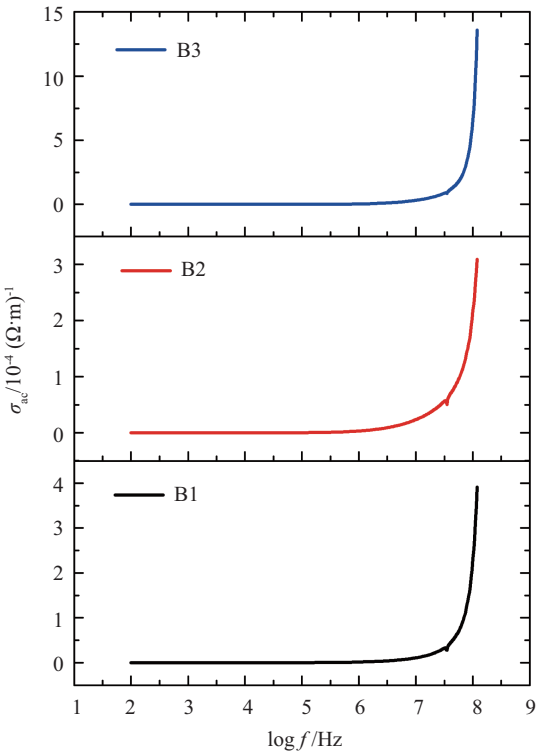


Fig. 11. (color online) AC conductivity for $Ba_{1-x}Dy_xFe_{12-y}Cr_yO_{19}$ ($x = 0.0, 0.1, 0.2$, and $y = 0.0, 0.4, 0.5$).

5. Conclusion

We have successfully prepared hexaferrites using the sol–gel method and AR grade starting materials. The solubility of the substituted ions in the hexaferrites up to B3 (*i.e.*, $x = 0.2$ and $y = 0.5$) can be assumed to be 100% because no secondary phase or impurity is observed in the XRD spectra. The band gap of the prepared samples depends on factors such as quantum confinement and crystallite sizes. The observed band gap is within the range of application in optoelectronics. All of the samples show dielectric properties that are typical of hexaferrites with low dielectric loss. The conductivity and dielectric constant of the prepared samples depends on electron hopping between Fe^{3+} and Fe^{2+} ions at octahedral site. The Cole–Cole plot shows that the contribution to the dielectric properties mostly comes from R_{gb}. It has been observed that, under the influence of applied electric field, the relaxation of defects dipoles displays a decreasing behavior with an increase in frequency and subsequently decreases the $\tan\delta$ in the higher frequencies region. The studies of hexaferrites carried out in this research have provided us with tuned properties that may be useful for technological application, such as in high frequency electronics devices.

Acknowledgement

The authors would like to thank Sophisticated Test and Instrumentation and Centre (STIC), Cochin University of Science and Technology, Kerala, India for UV-Vis-NIR Spectrophotometer characterization and Materials Research Centre (MRC), Malaviya National Institute of Technology (MNIT), Jaipur, India for impedance analyzer.

References

[1] Mohammed J, Suleiman A B, Hafeez H Y, Trudel T C T, Sharma J, Bhadu G R, Godara S K and Srivastava A K 2018 *Mater. Res. Express* **5** 086106
[2] Sharma J, Mohammed J, Kaur R, Trudel T C T and Srivastava A K 2017 *AIP Conf. Proc.* **1860** 020017
[3] Sharma J, Mohammed J, Trudel T C T and Srivastava A K 2017 *AIP Conf. Proc.* **1860** 020016
[4] Sharma J, Basandrai D and Srivastava A K 2017 *Chin. Phys. B* **26** 116201
[5] Basandrai D, Bedi R K, Dhami A, Sharma J, Narang S B, Pubby K and Srivastava A K 2017 *Chin. Phys. Lett.* **34** 044101
[6] Ma Y, Zhai K, Yan L, Chai Y, Shang D and Sun Y 2018 *Chin. Phys. B* **27** 027501
[7] Bahadur A, Saeed A, Iqbal S, Shoaib M, Ahmad I, Saif M, Bashir M I, Yaseen M and Hussain W 2017 *Ceram. Int.* **43** 7346
[8] Ma X M, Liu J, Zhu S Z and Shi H G 2016 *Chin. Phys. B* **25** 126102
[9] Trukhanov A, Panina L, Trukhanov S, Turchenko V and Salem M 2016 *Chin. Phys. B* **25** 016102
[10] Mohammed J, Sharma J, Kumar S, Trudel T T C and Srivastava A K 2017 *AIP Conf. Proc.* **1860** 020007
[11] Kaur T, Kumar S, Bhat B H and Srivastava A K 2015 *J. Mater. Res.* **30** 2753
[12] Kaur T, Kumar S, Bhat B H, Want B and Srivastava A K 2015 *Appl. Phys. A* **119** 1531
[13] Ashiq M N, Iqbal M J, Najamulhaq M, Gomez P H and Qureshi A M 2012 *J. Magn. Magn. Mater.* **324** 15
[14] Kuruva P, Matli P R, Mohammad B, Reddigari S and Katlakunta S 2015 *J. Magn. Magn. Mater.* **382** 172
[15] El-sayed S M, Meaz T M, Amer M A and El Shersaby H A 2013 *Physica B: Condens. Matter* **426** 137
[16] Ashiq M N, Iqbal M J and Gul I H 2009 *J. Alloys Compd.* **487** 341
[17] Kaur T, Sharma J, Kumar S and Srivastava A K 2017 *Cryst. Res. Technol.* **52** 1700098
[18] Auwal I A, Güner S, Güngüne H and Baykal A 2016 *Ceram. Int.* **42** 12995
[19] Kiani E, Rozatian A S H and Yousefi M H 2015 *J. Magn. Magn. Mater.* **361** 25
[20] Nandi S K, Nath S K, Akther Hossain A K M and Khan J U 2014 *J. Supercond. Nov. Magn.* **27** 2655
[21] Dhage V N, Mane M L, Keche A P, Birajdar C T and Jadhav K M 2011 *Physica B: Condens. Matter* **406** 789
[22] Wagner T R 1998 *J. Solid State Chem.* **136** 120
[23] Chawla S K, Mudsainiyan R K, Meena S S and Yusuf S M 2014 *J. Magn. Magn. Mater.* **350** 23
[24] Kaur T, Kaur B, Bhat B H, Kumar S and Srivastava A K 2015 *Physica B: Condens. Matter* **456** 206
[25] Kumar S, Kaur T, Kumar S and Srivastava A K 2015 *J. Supercond. Nov. Magn.* **28** 2935
[26] Nikmanesh H, Moradi M, Bordbar G H and Alam R S 2016 *Ceram. Int.* **42** 14342
[27] Baniasadi A, Ghasemi A, Nemati A, Ghadikolaei M A and Paimozd E 2014 *J. Alloys Compd.* **583** 325
[28] Rostami M, Moradi M, Alam R S and Mardani R 2016 *Mater. Res. Bull.* **83** 379
[29] R S Alam, Moradi M, Rostami M, Nikmanesh H, Moayedi R and Bai Y 2015 *J. Magn. Magn. Mater.* **381** 1

[30] Asiri S, Güner S, Korkmaz A D, Amir M, Batoo K M, Almessiere M A, Gungunes H, Sözeri H and Baykal A 2018 *J. Magn. Magn. Mater.* **451** 463
[31] Meena R S, Bhattachrya S and Chatterjee R 2010 *Mater. Sci. Eng. B* **171** 133
[32] Meena R S, Bhattachrya S and Chatterjee R 2010 *J. Magn. Magn. Mater.* **322** 2908
[33] Ali I, Ahmad M, Islam M U and Awan M S 2013 *J. sol-gel Sci. Technol.* **68** 141
[34] Bhargava R and Khan S 2017 *Adv. Powder Technol.* **28** 2812
[35] Heczko O, Gerber R and Simsa Z 2000 *Thin Solid Films* **358** 206
[36] Elghanem H M, Jawad S A, Aljundi J, Afaneh F and Arafa I 2003 *Polym. Int.* **52** 1125
[37] Odeh I, El Ghanem H M, Mahmood S H, Azzam S, Bsoul I and Lehlooh A F 2016 *Physica B: Condens. Matter* **494** 33
[38] Khare A, Sundar S, Mandal K D and Mukhopadhyay N K 2016 *Microelectron. Eng.* **164** 1
[39] Ashiq M N, Qureshi R B, Malana M A and Ehsan M F 2015 *J. Alloys Compd.* **651** 266
[40] Narang S B, Kaur D and Pubby K 2016 *Microw. Opt. Technol. Lett.* **58** 1679
[41] Jassal A K, Mudsainiyan R K, Chawla S K, Anu, Narang S B and Pubby K 2018 *J. Magn. Magn. Mater.* **447** 32
[42] Thongbai P, Jumpatam J, Putasaeng B, Yamwong T and Maensiri S 2014 *Mater. Res. Bull.* **60** 695
[43] Soman V V, Nanoti V M and Kulkarni D K 2013 *Ceram. Int.* **39** 5713
[44] Lalegani Z and Nemati A 2015 *J. Mater. Sci.: Mater. Electron.* **26** 2134
[45] Ali I, Islam M U, Awan M S and Ahmad M 2013 *J. Mater. Eng. Perform.* **22** 2104
[46] Hooda A, Sanghi S, Agarwal A and Dahiya R 2015 *J. Magn. Magn. Mater.* **387** 46
[47] Want B, Bhat B H and Ahmad B Z 2014 *J. Alloys Compd.* **627** 78
[48] Pubby K, Chawla S K, Kaur P, Kaur G and Bindra S B 2016 *Ferroelectrics* **505** 67
[49] Pubby K, Narang S B, Chawla S K and Mudsainiyan R K 2016 *J. Mater. Sci. Mater. Electron.* **27** 11220
[50] Malana M A, Qureshi R B, Ashiq M N and Ehsan M F 2016 *Ceram. Int.* **42** 2686